Nanoscale

ROYAL SOCIETY OF CHEMISTRY

COMMUNICATION

View Article Online
View Journal | View Issue



Cite this: *Nanoscale*, 2020, **12**, 16414

Received 22nd May 2020,
Accepted 10th July 2020

DOI: 10.1039/d0nr03948a

rsc.li/nanoscale

# A combination of an organic alloy and a heterojunction towards a rod–tail helix architecture with dual-color-emitting properties†

Hongyang Zhang, [a,b] Haitao Wang,[b] Peng-Cheng Qian [*c] and Wai-Yeung Wong [*a,b]

**An organic alloy can be regarded as a homogeneous solid solution wherein an isostructural molecule is randomly distributed in a host molecule, compared to an organic heterojunction where dissimilar materials generate an interface between two layers or regions. Herein, we fabricate an unprecedented novel BA@$BA_{0.72}BN_{0.28}$ heterostructure with a rod–tail helix configuration, in which the helical dual-component $BA_{0.72}BN_{0.28}$ alloy can be grown in a controllable manner onto the mono-component BA microrod, forming an organic core–shell micro-structure. In particular, the process of co-assembly formed could be described as the combined construction of an organic alloy and a heterojunction, and the co-assembly possesses the distinctive property of dual-color luminescence. This complex heterostructured architecture is achieved through a stepwise seed-induced growth method and the present solution-phase route allows us to construct more sophisticated organic luminescent heterostructured materials.**



## 1. Introduction

Organic heterojunction has always been an attractive research topic on account of its unique properties and superior performance when used in lasers,[1] bipolar transistors,[2] field effect transistors,[3] solar cells[4] and organic light-emitting devices.[5] Notably, the construction of heterojunctions at the nano- or micro-scale is an emerging field and remains a great challenge owing to the complicated dynamic assembly feature of each of the organic components. The process of fabrication is associated with the precise spatial manipulation of different constituent materials. The resultant heterojunction possesses a nano- or micro-scaled structural feature with the realization of increasingly elaborate performance, due to the synergistic effects with predefined constituent distribution.[6] On the other hand, an organic alloy could be regarded as a homogeneous solid mixture, and specifically, isostructural organic guest molecules are randomly dispersed in the crystal lattice of organic host molecules over a wide range of proportions.[7] This not only can unite the advantages of each organic component but also can confer improved and/or unexpected properties *via* a broad and continuous variation in chemical composition. For example, organic alloys of $TSeF_xTTF_{1-x}TCNQ$ were synthesized by the substitution of a TTF donor with another isostructural TSeF donor, and the value of $x$ is allowed to vary from 0 to 1 to achieve variable electrical properties.[8] Applying a supramolecular approach to prepare three- or four-component organic alloys and further investigation on the modulation of their physical properties by gradual alteration of the constituent ratio were also reported.[9] Moreover, organic alloys can also be applied in the organic thin film transistors (OFETs) with ambipolar performance as well as organic solar cells (OSCs).[10]

Controlled synthesis of a sophisticated heterogeneous architecture remains a great challenge, especially for organic constituent materials. Actually, great efforts have been made in this area. For instance, linear heterostructured nanotubes with dissimilar semiconducting properties were achieved by the stepwise assembly of two graphene derivatives.[11] Moreover, crystalline heterojunction nanorods composed of Ir(**III**) and Ru(**III**) metallophosphors were developed *via* a similar stepwise growth approach.[12] Recently, our group has achieved the controlled formation of supramolecular core–shell heterostructures with multicolor optical performance[13] as well as facet-selective growth of organic heterostructured architectures by sequential crystallization.[14] In previous works, it has been

[a]*Department of Applied Biology and Chemical Technology, The Hong Kong Polytechnic University, Hung Hom, Hong Kong, China. E-mail: wai-yeung.wong@polyu.edu.hk*
[b]*Department of Chemistry, Hong Kong Baptist University, Waterloo Road, Hong Kong, China*
[c]*Key Laboratory of Environmental Functional Materials Technology and Application of Wenzhou City, Institute of New Materials & Industry, College of Chemistry & Materials Engineering, Wenzhou University, Wenzhou 325035, China. E-mail: qpc@wzu.edu.cn*

†Electronic supplementary information (ESI) available: Experimental details, SEM images and molecular packing of single crystals. See DOI: 10.1039/d0nr03948a

revealed that choosing structurally compatible materials and appropriately tuning their growth kinetics is the key to construct complex organic heterostructures.

The integration of an organic alloy into an organic heterojunction has been rarely reported due to the difficulty in simultaneously producing the alloy and controlling the growth kinetics of the alloy on the seeded material. Herein, based on the complex assembly from planar and twisted π-conjugated molecules to obtain the organic alloy,[15] we further develop an unprecedented heterogeneous rod–tail helix configuration, *i.e.* BA@$BA_{0.72}BN_{0.28}$, with a core–shell structure constructed by a two-step seed-induced growth approach. The organic alloy shell is composed of two isostructural semiconductor molecules, BA and BN, through π–π interactions. In contrast to the dual-component shell, the core rod comprises a single BA molecule. During the formation process, the alloy shell $BA_{0.72}BN_{0.28}$ first deposits on the side face of the BA core *via* solution epitaxial growth,[17] then the ribbon-shaped shell extends out with screwing into bundles of helix, and finally forming the structure with the rod–tail helical shape.

## 2. Results and discussion

Two structurally similar π-conjugated molecules, 9,10-bis(phenylethynyl)anthracene (BA) and 5,12-bis(phenylethynyl) naphthacene (BN) (Fig. 1a), are chosen to explore the fabrication of an organic alloy as well as its novel heterostructure. Under specific preparation conditions (v/v = 4 : 1, an ethanol/$H_2O$ solvent mixture), the individual assemblies of these two isostructural molecules possess two slightly different morphologies. Specifically, BA can assemble into partial hollow microrods (Fig. 1b and e and Fig S1, ESI†), while BN can assemble into hollow microtubes (Fig. 1c and f). By contrast, BA and BN can co-assemble into organic alloy helices (Fig. 1d, g & Fig S2, ESI†) under the same synthetic conditions because the BA–BN dimeric units can be consistently twisted towards one joint direction which would be a preferable strategy of decreasing the total free energy in the co-assembly system. The BN guest can occupy the sites in which the BA host provides and forms the specific composition $BA_{0.72}BN_{0.28}$, which has been confirmed in our previous work.[15]

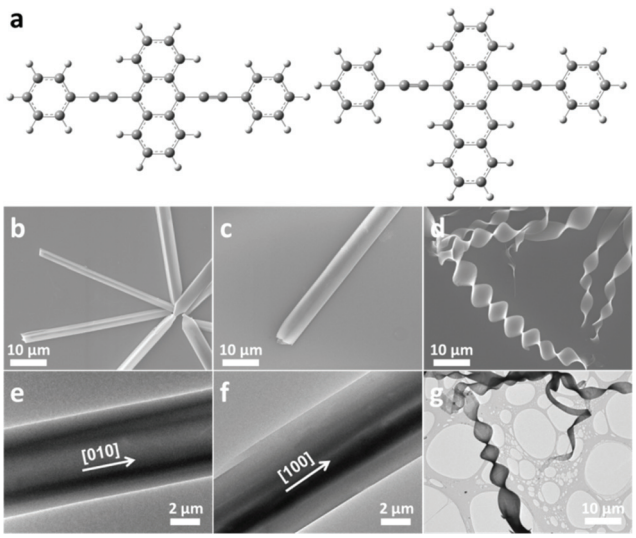


**Fig. 1** (a) Schematic illustration of the BA and BN molecular structures. (b and e) SEM and TEM images of microrods composed of a single component: BA. (c and f) SEM and TEM images of microtubes composed of a single component: BN. (d and g) SEM and TEM images of organic alloy helices composed of BA and BN components: $BA_{0.72}BN_{0.28}$.

Instead of fabricating a simple core–shell structure by applying a simple solute exchange method, a complex core–shell structure, BA@$BA_{0.72}BN_{0.28}$, was designed and developed here *via* a stepwise seed-induced growth method. The growth mechanism can be explicated by the epitaxy process besides the structural analyses of the BA crystal and the BA/BN alloy crystal (Fig. S4a and b, ESI†). As we have investigated previously, it is hard to recognize BN molecules from the crystal lattice of BA in alloys because BN molecules would be randomly located at the sites provided by BA hosts, and thus the two-component organic alloy crystal exhibits a similar molecular configuration relative to the pure BA crystal, in which planar BA and twisted BN molecules are stacked together by strong π–π interactions (Fig. S4c and d, ESI†).[16] Reasonably, the mono-component molecular stacking mode favors the formation of the 1D morphology, therefore with the existence of a BA rod-like seed and the good match between the lattices of the seed and the second growing alloy constituent, the first step, epitaxial growth occurs,[17] with the ribbon-shaped alloy shell $BA_{0.72}BN_{0.28}$ growing on the BA seed entirely with the remaining shown as the rod figure. Next, the second step occurs, the surplus shell would extend out and it would be influenced by its own intermolecular force for recurring into a helical shape, finally leading to the core–shell construction of the rod–tail helix architecture (Fig. 2). Here, the intermolecular force refers to the consistent twisting of BA–BN dimeric units towards the same direction, thereby resulting in a helical superstructure for the sake of reducing the total free energy in the alloy system.[18]

During the detailed preparation process, the pre-synthetic BA microrods acted as the seed and were dispersed under the same synthetic conditions for all of these self- and co-assemblies (v/v = 4 : 1, ethanol/$H_2O$ solvent mixture, 5 mL). By means of fast injection of 1 mL of stock solution of BA/BN in THF with a 2 : 1 molar ratio ($C_{BA}$ = 5 mM, $C_{BN}$ = 2.5 mM) and then gentle shaking of the mixed solution, a large number of heterogeneous core–shell microstructures, BA@$BA_{0.72}BN_{0.28}$, would be synthesized in the solution system (Fig. 3a). SEM characterization shows the specific topological configuration (Fig. 3b and c). From the TEM images (Fig. 3d and e), we could compare the thickness of the outside shell with the diameter of the inside core, which is about 1 : 1 in the length ratio (More SEM and TEM images of BA@$BA_{0.72}BN_{0.28}$ are shown in Fig. S5, ESI.†). Besides, in order to get more direct evidence to identify the core–shell fabrication, fluorescence microscopy tests were performed to examine the configuration because the

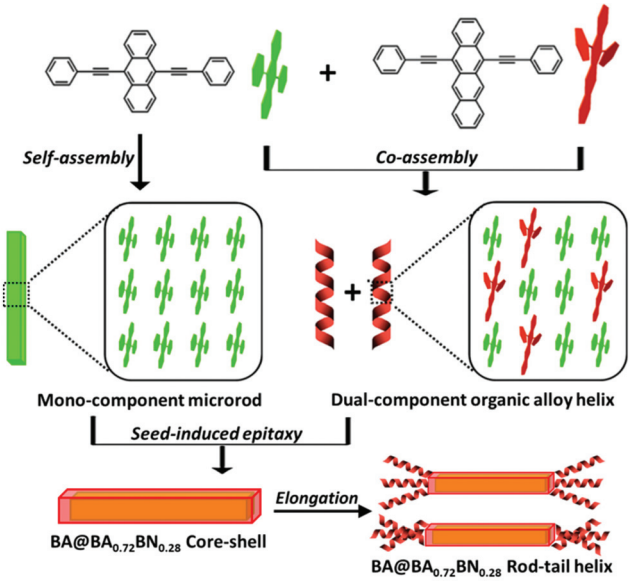


**Fig. 2** Schematic illustration of the growth mechanism of the $BA@BA_{0.72}BN_{0.28}$ rod–tail helix and the molecular packing of the $BA_{0.72}BN_{0.28}$ alloy helix, in which the BA host molecules are randomly replaced by the BN molecules and a BA–BN dimeric structure with a slight twist is formed.

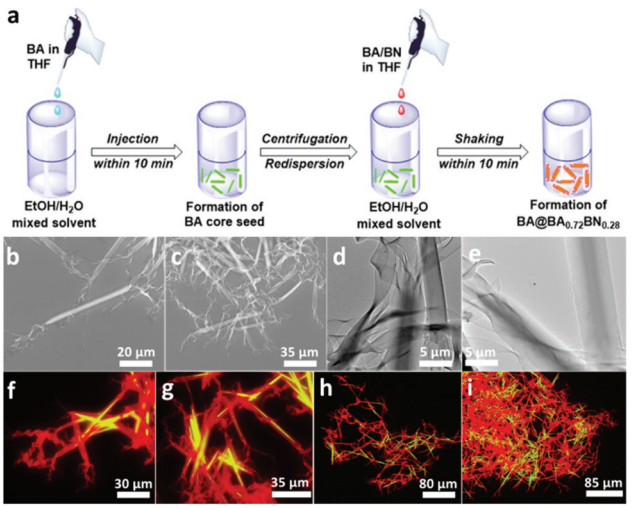


**Fig. 3** (a) Schematic illustration of the synthetic procedure of the $BA@BA_{0.72}BN_{0.28}$ rod–tail helix. (b–c) SEM images of the $BA@BA_{0.72}BN_{0.28}$ rod–tail helix (viewed from single to multiple). (d–e) TEM images of the $BA@BA_{0.72}BN_{0.28}$ rod–tail helix (viewed from tail to rod). (f–i) Fluorescence microscopy images of the $BA@BA_{0.72}BN_{0.28}$ rod–tail helix upon excitation with the blue laser (viewed from small to large).

core and shell can be distinguished by their different emission colors. Fig. 3f and g show the corresponding FM images excited by a blue laser, and as expected, the red-emitting layer is deposited onto the surface of a green-emitting core. The elongated helical ribbon emits the same color of light as that of the shell layer covered on the core rod. From a wider point of view, we can see that this is not a specially observed sample on a partial position, but a general phenomenon throughout the whole domain (Fig. 3h and i).

In order to fully investigate the distinctions of these assemblies and co-assemblies, their photophysical properties were first measured. With the aid of solid photoluminescence spectra, we can see that the emission band of the $BA_{0.72}BN_{0.28}$ alloy (665 nm) is located between the emission bands of BA microrods (550 nm) and BN microtubes (710 nm). Notably, the PL spectrum of the $BA@BA_{0.72}BN_{0.28}$ core–shell structure can be regarded as the spectral superposition of the separated BA assembly and $BA_{0.72}BN_{0.28}$ alloy (Fig. 4a). This result not only confirms the core–shell fabrication but also implies the content of BA and $BA_{0.72}BN_{0.28}$ depending on their luminescence intensities. The emission and excitation spectra of BA monomer solution, BN monomer solution and BA/BN precursor solutions in different concentrations (Fig. S6 & S7, ESI†) were also recorded to demonstrate the strong π–π interaction among these π-conjugated molecules, and the details are discussed in the ESI.† Then, the powder X-ray diffraction (XRD) tests of these four assemblies were performed to reveal the internal structural information. Obviously, the XRD pattern of the $BA_{0.72}BN_{0.28}$ helix (Fig. 4b, blue curve) exhibits a pattern of the newly formed crystal phase, which is different from that of pure BA (Fig. 4b, red curve) and BN (Fig. 4b, black curve). Newly generated peaks at 7.6° and 10.4° not only indicate high-quality crystallinity but also reveal the alloy nature of the crystal phase. Then, for the pattern of the rod–tail helix heterostructure, $BA@BA_{0.72}BN_{0.28}$, the superimposed peaks that overlap are attributed to BA and $BA_{0.72}BN_{0.28}$, and therefore this also can be looked upon as the direct evidence of the formation of a heterostructured architecture. Furthermore, we explored their thermal stabilities and found that the decomposition temperature of pure BA is higher than that of the organic alloy $BA_{0.72}BN_{0.28}$, probably due to a small amount of BN molecules incorporated into the alloy system whose thermal stability is slightly inferior to that of the BA molecule.

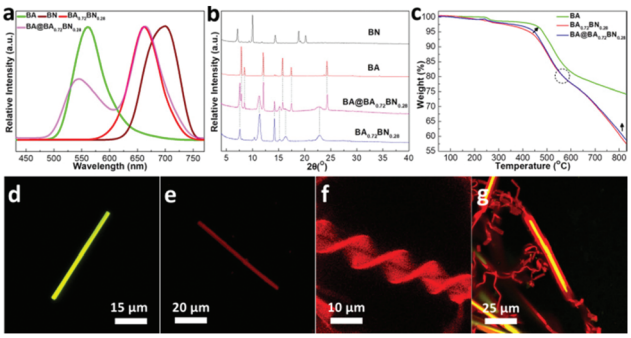


**Fig. 4** (a) Solid-state emission spectra of BA, BN, $BA_{0.72}BN_{0.28}$ and $BA@BA_{0.72}BN_{0.28}$ assemblies upon excitation with the blue laser ($\lambda_{ex}$ = 405 nm), (b) powder XRD patterns of BA, BN, $BA_{0.72}BN_{0.28}$ and $BA@BA_{0.72}BN_{0.28}$ assemblies, (c) thermogravimetric analysis (TGA) plots of BA, $BA_{0.72}BN_{0.28}$, and $BA@BA_{0.72}BN_{0.28}$ assemblies, (d–g) laser confocal fluorescence microscopic (LCFM) images of the BA rod, BN tube, $BA_{0.72}BN_{0.28}$ helix and $BA@BA_{0.72}BN_{0.28}$ rod–tail helix.

The TGA plot of BA@$BA_{0.72}BN_{0.28}$ is exactly situated between the curves of separate BA and $BA_{0.72}BN_{0.28}$, suggesting that the composition of the rod–tail helix heterojunction is just the combination of two materials, which is the indirect evidence of the formation of the heterostructured architecture (Fig. 4c). Then, laser confocal fluorescence microscopy (LCFM) is employed to record the shape, emission and morphology of the BA microrod (Fig. 4d), the BN microtube (Fig. 4e), the $BA_{0.72}BN_{0.28}$ helix (Fig. 4f) and the BA@$BA_{0.72}BN_{0.28}$ rod–tail helix (Fig. 4g), respectively. By sight, the construction of the heterostructured architecture can be directly perceived.

Laser confocal fluorescence microscopy (LCFM) was further applied to evaluate the formed core–shell heterojunction from both qualitative and quantitative perspectives. The individual records of emission on the core (Fig. 5b and e) and the shell (Fig. 5c and f) were conducted, respectively, and their merged emitting images were also provided (Fig. 5a and d). As we recorded the green light emitted from the core rod, the luminescence signal from the outside shell could not be detected, while as we collected the red emission of the shell layer, the emission of the inside core would disappear. The corresponding micro-area PL spectrum of BA@$BA_{0.72}BN_{0.28}$ at the core–shell junction (marked in the white rectangle, Fig. 5d) shows a PL peak at 546 nm in the short-wavelength range and a PL peak at 665 nm in the long-wavelength range, which is exactly the superposition of the peaks of a separate BA rod and a BA/BN alloy. The intensities of the emission peaks also imply the content of two components on the whole heterostructure (Fig. 5g). By focusing on the PL peak on the middle section of the core–shell structure (marked in the white rectangle, Fig. 5e), we found that it shares the analogous spectral profile of two peaks but with different peak intensities. The PL peak at 546 nm caused by the inner BA core is higher than the peak at 661 nm derived from the outer shell. This not only indicates that the middle section is composed of two constituent materials, but also gives the information of composition variation, in which the BA content rises at the middle section (Fig. 5h). Regarding the micro-area PL spectrum at the tip tail (marked in the white rectangle, Fig. 5f), it is the typical profile of the BA/BN alloy helix with a single peak at 663 nm (Fig. 5i). Therefore, the above results adequately testify to the formation of the BA@$BA_{0.72}BN_{0.28}$ core–shell heterostructure.

Additionally, we selected a locally enlarged position using laser confocal fluorescence microscopy (LCFM, Fig. 6a–c) and took the emission images to record the continuously varying process of increasing the emission wavelength at 500, 550, 600, 650 and 700 nm respectively, in which the output signal was modified to the corresponding emitting color (Fig. 6d). Obviously, the emission range of the inner core is concentrated at 550 nm. By comparison, the emission range of the outer shell and the tail helix are focused at around 650 nm. In the transitional region at 600 nm, basically no emitting materials can be seen by eye, while the emissions are relatively weak at 500 and 700 nm as well. The emitting properties of the specific wavelengths are in accordance with the feature of the heterostructure. Thus far, the current characterization studies have comprehensively supported the successful growth of the dual-component organic alloy helix onto the mono-component microrod towards the rod–tail helix heterostructure from qualitative, quantitative, static and dynamic perspectives. Moreover, the organic helical organization is expected to exhibit superior optoelectronic performance,[19] such as for circularly polarized luminescence (CPL).[20] Although both left- and right-handed helices are found in our prepared system (Fig. S2b, ESI†), the final product should be a racemic mixture because achiral BA and BN were used as the building blocks. The circular dichro-

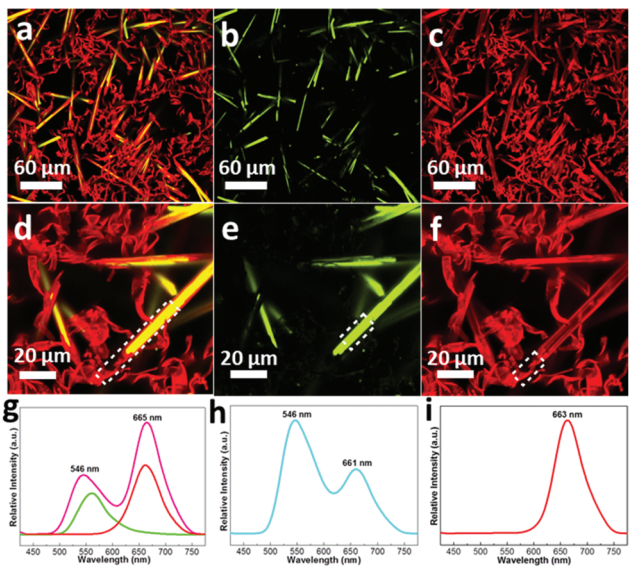


Fig. 5 (a–c) LCFM images of the core–shell rod–tail helix heterojunction BA@$BA_{0.72}BN_{0.28}$ at low magnification when collecting the green-light, red-light, and the merged emitting image, respectively; (d–f) LCFM images of the core–shell rod–tail helix heterojunction BA@$BA_{0.72}BN_{0.28}$ at high magnification when collecting the green-light, red-light, and the merged emitting image, respectively; (g–i) micro-area PL spectra recorded from the selected areas on the rod–tail helix heterojunction BA@$BA_{0.72}BN_{0.28}$ marked in the white rectangle in (d–f).

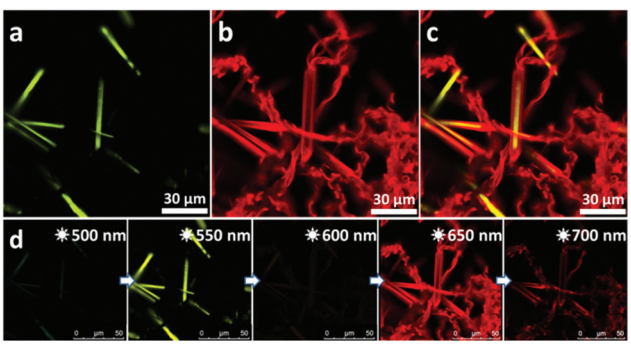


Fig. 6 (a–c) Locally enlarged LCFM images of the core–shell rod–tail helix: BA@$BA_{0.72}BN_{0.28}$ when collecting green-light, red-light and the merged image of emission, respectively. (d) Emission images as a function of increasing wavelength.

ism (CD) spectrum also reveals the presence of a racemic mixture (Fig. S3, ESI†). It will be of great interest to explore CPL based on the separation of chiral helices, and further work will be focused on this potential application in the opto-electronic field.

## 3. Conclusions

A complex organic heterostructure with the novel topological configuration was designed and fabricated through a stepwise seed-induced assembly process, wherein the organic alloy $BA_{0.72}BN_{0.28}$ would wrap up the BA seed and spread out at the tip to turn it into its original helical morphology, which finally forms the rod–tail helix architecture. The random occupancy of the twisted BN guest at the sites of the BA host has little effect on the configuration of intermolecular stacking. This enables the perfect lattice matching between BA and $BA_{0.72}BN_{0.28}$ and provides the possibility for the desired growth of the organic alloy on the preformed mono-component seed. The present successful case for constructing the elaborated heterostructure sets up a bridge between the organic alloy and the organic heterojunction, and it could let us harness the advantages of both materials. As an inspiration, this synthetic approach also provides a promising platform to understand the structural relationship among varied but congenetic organic materials and can be considered as a general pathway for realizing more sophisticated heterostructured architectures.

## Conflicts of interest

The authors declare no competing financial interest.

## Acknowledgements

W.-Y. W. acknowledges the financial support from the Hong Kong Research Grants Council (PolyU153062/18P), the Hong Kong Polytechnic University (1-ZE1C) and Ms Clarea Au for the Endowed Professorship in Energy (847S). P. C. Q. thanks the Foundation of Wenzhou Science & Technology Bureau (No. W20170003) and the National Natural Science Foundation of China (No. 21828102).

## Notes and references

1 H. Kroemer, *Proc. IEEE*, 1963, **51**, 1782–1783.
2 (*a*) G. L. Patton, S. S. Iyer, S. L. Delage, S. Tiwari and J. M. C. Stork, *Proc. IEEE*, 1988, **9**, 165–167; (*b*) S. S. Iyer, G. L. Patton, J. M. C. Stork, B. S. Meyerson and D. L. Harame, *Proc. IEEE*, 1989, **36**, 2043–2064.
3 (*a*) Y. F. Wu, B. P. Keller, S. Keller, D. Kapolnek, P. Kozodoy, S. P. Denbaars and U. K. Mishra, *Appl. Phys. Lett.*, 1996, **69**, 1438–1440; (*b*) J. Wang, H. B. Wang, X. J. Yan, H. C. Huang and D. H. Yan, *Appl. Phys. Lett.*, 2005, **87**, 093507.
4 (*a*) A. Hagfeldt, G. Boschloo, L. C. Sun, L. Kloo and H. Pettersson, *Chem. Rev.*, 2010, **110**, 6595–6663; (*b*) A. J. Heeger, *Adv. Mater.*, 2014, **26**, 10–28; (*c*) Y. Huang, E. J. Kramer, A. J. Heeger and G. C. Bazan, *Chem. Rev.*, 2014, **114**, 7006–7043.
5 (*a*) C. W. Tang, S. A. VanSlyke and C. H. Chen, *J. Appl. Phys.*, 1989, **65**, 3610–3616; (*b*) S. Wang, H. Zhang, B. Zhang, Z. Xie and W. Y. Wong, *Mater. Sci. Eng., R*, 2020, **140**, 100547.
6 (*a*) F. Huang and E. V. Anslyn, *Chem. Rev.*, 2015, **115**, 6999–7000; (*b*) M. A. Boles, M. Engel and D. V. Talapin, *Chem. Rev.*, 2016, **116**, 11220–11289; (*c*) S. Leininger, B. Olenyuk and P. J. Stang, *Chem. Rev.*, 2000, **100**, 853–908; (*d*) G. M. Whitesides and B. Grzybowski, *Science*, 2002, **295**, 2418–2421.
7 (*a*) M. D. Gujrati, N. S. S. Kumar, A. S. Brown, B. Captain, J. N. Wilson, E. M. Engler, B. A. Scott, S. Etemad, T. Penney and V. V. Patel, *J. Am. Chem. Soc.*, 1977, **99**, 5909; (*b*) R. Natarajan, G. Magro, L. N. Bridgland, A. Sirikulkajorn, S. Narayanan, L. E. Ryan, M. F. Haddow, A. G. Orpen, J. P. H. Charmant, A. J. Hudson and A. P. Davis, *Angew. Chem., Int. Ed.*, 2011, **50**, 11386; (*c*) J. Q. Zhang, Y. J. Zhang, J. Fang, K. Lu, Z. Y. Wang, W. Ma and Z. X. Wei, *J. Am. Chem. Soc.*, 2015, **137**, 8176; (*d*) M. Dabros, P. R. Emery and V. R. Thalladi, *Angew. Chem., Int. Ed.*, 2007, **46**, 4132; (*e*) K. Sada, K. Inoue, T. Tanaka, A. Epergyes, A. Tanaka, N. Tohnai, A. Matsumoto and M. Miyata, *Angew. Chem., Int. Ed.*, 2005, **44**, 7059.
8 E. M. Engler, B. A. Scott, S. Etemad, T. Penney and V. V. Patel, *J. Am. Chem. Soc.*, 1997, **99**, 5909–5916.
9 M. Dabros, P. R. Emery and V. R. Thalladi, *Angew. Chem.*, 2007, **119**, 4210–4213.
10 (*a*) X. M. Xu, T. Xiao, X. Gu, X. J. Yang, S. V. Kershaw, N. Zhao, J. B. Xu and Q. Miao, *ACS Appl. Mater. Interfaces*, 2015, **7**, 28019; (*b*) Y. Zhen, H. Tanaka, K. Harano, S. Okada, Y. Matsuo and E. Nakamura, *J. Am. Chem. Soc.*, 2015, **137**, 2247–2252.
11 W. Zhang, W. S. Jing, T. Fukushima, A. Saeki, S. Seki and T. Aida, *Science*, 2011, **334**, 340–343.
12 M.-J. Sun, Y. Liu, Y. Yan, R. Li, Q. Shi, Y. S. Zhao, Y.-W. Zhong and J. Yao, *J. Am. Chem. Soc.*, 2018, **140**, 4269–4278.
13 H. Zhang, Y. Lei, H. Wang and W.-Y. Wong, *J. Mater. Chem. C*, 2020, **8**, 2669–2675.
14 Y. Lei, Y. Sun, L. Liao, S. T. Lee and W.-Y. Wong, *Nano Lett.*, 2017, **17**, 695–701.
15 Y. Lei, Y. Sun, Y. Zhang, H. Zhang, H. Zhang, Z. Meng, W.-Y. Wong, J. Yao and H. Fu, *Nat. Commun.*, 2018, **9**, 4358.
16 (*a*) X. Xu, B. Shan, S. Kalytchuk, M. Xie, S. Yang, D. Liu, S. V. Kershaw and Q. Miao, *Chem. Commun.*, 2014, **50**, 12828–12831; (*b*) Y. Wu, J. Feng, X. Jiang, Z. Zhang, X. Wang, B. Su and L. Jiang, *Nat. Commun.*, 2015, **6**, 6737–6746; (*c*) C. Wang, Y. Liu, Z. Ji, E. Wang, R. Li, H. Jiang,

 

Q. Tang, H. Li and W. Hu, *Chem. Mater.*, 2009, **21**, 2840–2845.
17 (*a*) C. Xu, P. He, J. Liu, A. Cui, H. Dong, Y. Zhen, W. Chen and W. Hu, *Angew. Chem., Int. Ed.*, 2016, **55**, 9519–9523; (*b*) H. Dong, L. D. Sun, L. D. Li, R. Si, R. Liu and C. H. Yan, *J. Am. Chem. Soc.*, 2017, **139**, 18492–18495.
18 (*a*) M. H. Liu, L. Zhang and T. Y. Wang, *Chem. Rev.*, 2015, **115**, 7304–7397; (*b*) Y. Wang, J. Xu, Y. W. Wang and H. Y. Chen, *Chem. Soc. Rev.*, 2013, **42**, 2930–2962.
19 Q. Li and Z. Li, *Acc. Chem. Res.*, 2020, **53**, 962–973.
20 Y. Cheng, S. Liu, F. Song, M. Khorloo, H. Zhang, T. K. Kwok, W. Y. Lam, Z. He and B. Z. Tang, *Mater. Horiz.*, 2019, **6**, 405–411.